The Formation and Breakup of Molten Oxide Jets Under Periodic Excitation

Mirco Wegener, Luckman Muhmood, Shouyi Sun, and Alex V. Deev
CSIRO Process Science and Engineering, Box 312 Clayton South, Victoria 3169, Australia

DOI 10.1002/aic.14485

The experiments on the capillary breakup of slag jets at high temperatures are presented in this article. The impact of external excitations on the disintegration process was investigated in a furnace with optical access filmed at frame rates up to 10,000 fps. A synthetic calcia-alumina slag was used to form jets at different temperatures (1570–1660°C) and jet velocities (0.6–1.4 ms^{-1}). The impact of external vibration on the breakup was evident: for low jet velocities, the jet length decreased, the droplet size increased, satellite droplet formation was hindered, and a distinct "pumping mechanism" was observed. For jets with higher velocity, the jet length decreased by 30%, the droplet generation frequency increased from 20 to 250 droplets per second, the drop sizes were uniform, and satellite formation was also suppressed. In this case, the ideal case in which the volume of one wave instability forms one droplet was achieved. © 2014 American Institute of Chemical Engineers *AIChE J*, 60: 3350–3361, 2014

Keywords: slag, capillary breakup, surface tension, droplet formation, jet

Introduction

Jets, filaments, and threads of molten oxides or slags are of interest in a number of high-temperature applications. They are formed intentionally or unintentionally by the interplay of the involved phases: liquid metal, slag, and/or gas. For example, splashing occurs in the basic oxygen furnace where a supersonic gas jet impinges on the melt surface[1] and creates jets or filaments of molten material which finally breakup into droplet cascades. Richardson[2] gives examples of jet-like molten material ejection from metal droplets due to collapsing gas bubbles formed by a chemical reaction at high temperatures. In an after-treatment process for heat recovery from blast furnace slags – the dry slag granulation[3] – molten slag is poured onto a spinning disc to form filaments and/or sheets which breakup into droplets. The uniformity of the particle-size distribution plays a significant role in the succeeding heat exchanger stage. In inviscid melt spinning, the growth of such capillary instabilities on liquid calcia-alumina jets has to be avoided to facilitate continuous filaments.[4] The concept of liquid droplet heat exchangers (LDHX) – as proposed by Bruckner[5] although not yet realized – is based on the capillary breakup of multiple jets of molten slag into uniformly sized droplets to facilitate direct heat transfer to a counter-current gas stream.

The capillary breakup of low-temperature liquid jets (<500°C) in a gaseous environment has been studied theoretically and experimentally in a comprehensive manner. No literature seems to be available which deals with the dynamics of jet formation, wave instabilities, breakup, and finally droplet formation of high-temperature oxide melts. Hence, no direct experimental verification of existing theories and concepts of jet breakup is available for this group of high-viscosity/high-surface tension liquids. The source of instabilities which eventually triggers the breakup in jets with low velocity is the surface tension.[6,7] In this so-called Rayleigh breakup regime, gas effects can be neglected. More important is the relative magnitude of the competing gravitational, inertia, viscous, and capillary (surface tension) forces which governs the dynamics of instability. For example, if the capillary force is dominant compared to inertia (this force ratio is expressed by the Bond number), disturbances propagate both upstream and downstream. In the reversed case, inertia forces are dominant over surface tension forces and the disturbances only propagate in the downstream direction.[7] At same time, the Weber number which determines the fluid dynamic regime has to be considered, that is, dripping or jetting.

The exact characteristics and especially the origin of these disturbances are still unknown.[8] They can come from both interactions with the ambient surroundings and from the jet itself. Their growth very much depends on the working conditions and the above mentioned relative magnitude of forces in play.[8] According to Rayleigh, breakup occurs if the wavelength of the perturbation is longer than the circumference of the jet.[9] In the ideal case, the volume of the liquid contained within one wavelength of a disturbance will form one main drop.[10,11] Eggers and Villermaux[12] point out that the jet breakup mode depends on the amplitude of the initial perturbation in a highly sensitive manner. Therefore, a small deviation from the optimum frequency of the disturbance may lead to nonlinearities and one or more (and most likely undesirable) satellite droplets – depending on the fluid properties and the strength of the disturbance.[13] The ratio of the size of

---

Correspondence concerning this article should be addressed to Mirco Wegener at mirco.wegener@alumni.tu-berlin.de.

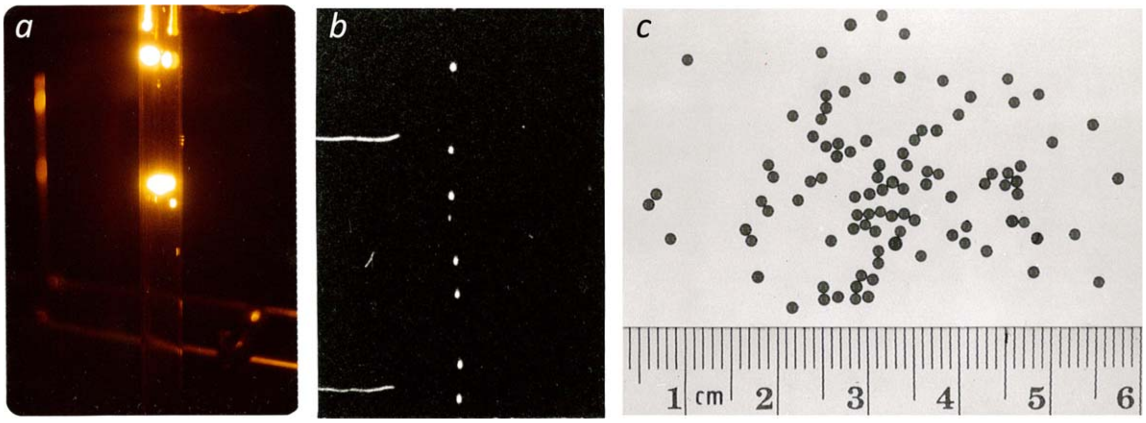

Figure 1. Slag droplet formation in Benda's experiments.[26]

(a) Slag globules resulting from improper jet formation. (b) High-speed images of droplets formed from externally disturbed jets. (c) Group of uniform solidified droplets produced by 335 Hz excitation. Droplet size range: 1.3–1.42 mm. Reproduced from Ref. 26, with permission from University of Washington. [Color figure can be viewed in the online issue, which is available at wileyonlinelibrary.com.]

the main droplet and the satellite droplet depends on the wavenumber.[14,15] Pimbley and Lee[16] give a map for conditions of satellite formation including a "no satellite region."

To control the jet breakup mode, an external perturbation is applied to minimize the effect of random disturbances. In literature, there are many examples using different techniques[6,11,17–25] The level of experimental and theoretical sophistication achieved for low-temperature systems is remarkable. Experiments are possible with a high degree of precision and control due to a relatively unproblematic physical and optical access to all components of the test facility. This becomes a serious issue as soon as the temperature is increased beyond the thermal stability of the commonly used materials, as this is the case for industrial slags with melting temperatures typically beyond 1400°C. The access to the capillary is restricted or even impossible.

To facilitate jet experiments at high temperatures, the uniform temperature zone has to be relatively long which imposes design and material restrictions. Hence, a custom made furnace has to be used whose dimensions can only be minimized to a certain degree. Also, depending on the molten material, the gaseous atmosphere has to be controlled in terms of oxygen. Dense alumina protection tubes are normally used to facilitate the required atmosphere and to homogenize the temperature field. Alumina is an opaque material, and optical access is only possible via x-ray or by cutting the tubes and extending the optical access horizontally using a second tube which is orthogonal to the vertical one. This imposes further restrictions such as the maximum length of the optically accessible path. Taking into considerations the above, mechanical vibration seems to be the most effective way to impose an external perturbation on the liquid jet of molten oxides.

Due to the complications and issues in high-temperature experiments, literature dealing with the experimental investigation of formation and breakup of molten oxide jets is scarce. Benda[26] investigated the breakup of a calcia-silica-magnesia-based slag. With his experimental setup, it was not possible to directly observe droplet and/or jet formation. However, some photographs are presented which show glowing globules and single falling droplets after jet breakup, see examples in Figure 1. Although the author had no possibility to observe the dynamics of formation and breakup directly, and although there were some issues concerning the determination of the capillary flow rate in a high-temperature environment, the experiments can be considered as valuable with regards to the feasibility and applicability of a controlled formation of slag droplets bearing in mind the demanding and complex issues evolving around experiments and materials behavior at these temperatures.

The present study continues the successful work of the two preceding articles[27,28] in which we reported for the first time the dynamics of formation and natural breakup of slag jets emerging from a graphite capillary at 1600°C under different flow conditions. This time, the impact of an imposed perturbation on jet formation, breakup, and drop size distribution is studied and compared to natural breakup and theoretical considerations. Slags or molten oxides exhibit a unique combination of physical properties, especially in the context of jet stability, which are reflected by the relatively high viscosity and surface tension values, and are, therefore, – from a fundamental point of view – an ideal test case to explore the breakup phenomena known otherwise only for low-temperature liquids.

Material and Methods

The experimental setup, see Figure 2, and procedure were similar to our preceding study. The main components were the same, such as (1) the electrically heated three zone tube furnace with optical access (Tetlow Kilns & Furnaces Pty Victoria, Australia), (2a,b) the 99.8% high-purity alumina cross tube assembly for optical access and atmosphere control (McDanel Advanced Ceramic Technologies, PA), (3) and (a–f) the droplet generating device made of graphite (Mersen Oceania Pty), and (4) the Phantom v3.11 high-speed camera. The main difference in the present study was the usage of a pneumatic turbine vibrator (22) to impose a controlled periodic excitation on the jet.

The three zone furnace (1) with a maximum temperature of 1750°C accommodated the alumina cross tube assembly – equipped with four water cooled end caps ($Q_{\mathrm{w,in}}$ and $Q_{\mathrm{w,out}}$) – required for optical access. This assembly was built using two individual tubes, one vertical (2a) and one horizontal tube (2b). The latter fitted through a corresponding opening in the vertical tube. The joints were properly sealed with a high-

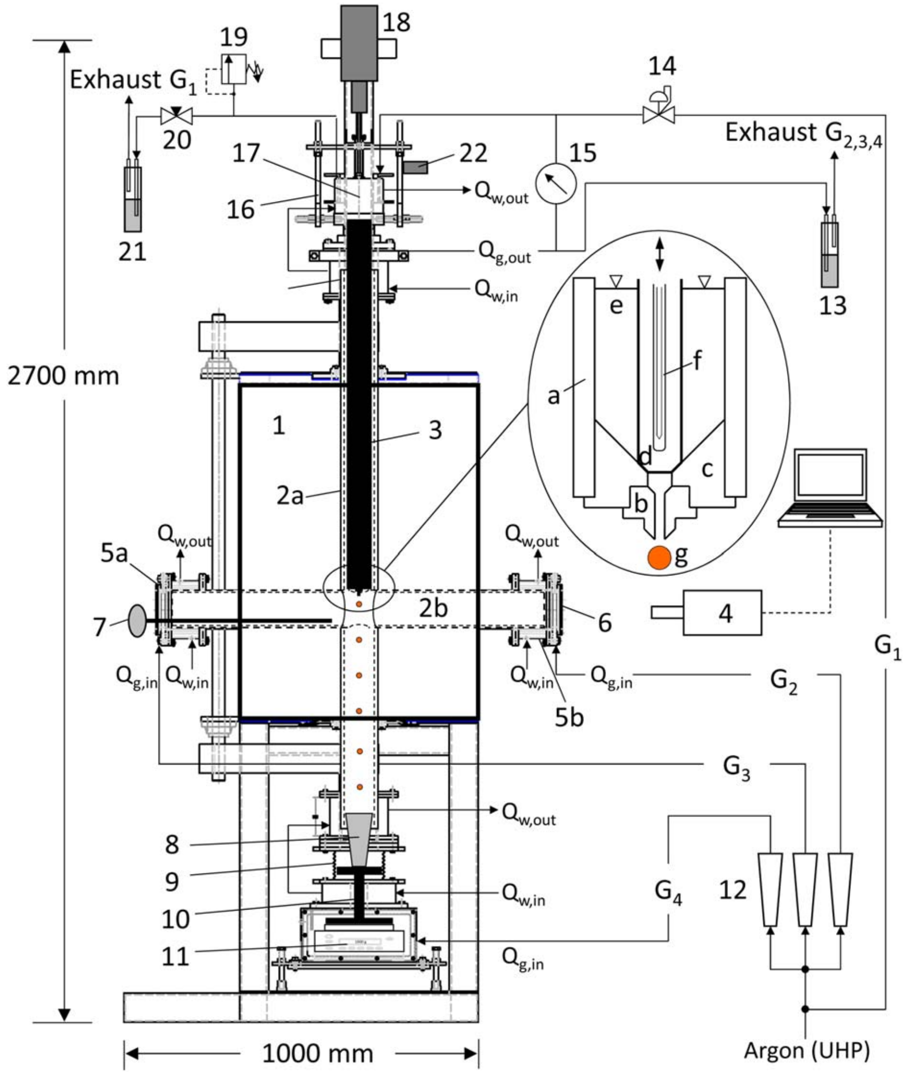

Figure 2. Schematic of the high-temperature three zone furnace and auxiliaries.

1: Heating chamber, 2a: Vertical alumina tube, 2b: Horizontal alumina tube, 3: Graphite crucible, shank section, a–g (zoom): Droplet generation device, a: Crucible hearth, b: Graphite capillary, c: Tapered bottom, d: Hollow graphite stopper, e: Slag, f: B-type thermocouple in alumina sheath, g: Slag droplet, 4: High-speed camera and computer, 5a,b: Water cooled end caps horizontal alumina tube, 6: Quartz window, 7: Oxygen probe with R-type thermocouple, 8: Stainless steel cup to collect slag droplets, 9: Metal bellows, 10: Graphite stand, 11: Balance chamber, 12: Gas rotameter, 13: Gas bubbler and exhaust alumina tube unit, 14: Precision pressure regulator, 15: Differential pressure transducer, 16: Graphite crucible lifting assembly, 17: Graphite shank water cooled end cap, 18: Precision linear actuator for stopper, 19: Safety relief valve, 20: Needle valve, 21: Gas bubbler and exhaust graphite crucible unit, 22: Pneumatic turbine vibrator. [Color figure can be viewed in the online issue, which is available at wileyonlinelibrary.com.]

temperature ceramic adhesive (Ceramabond 671, Aremco Products). Two 38 mm holes in the horizontal tube's center position allowed the slag droplets or jets (g) to fall from the graphite capillary (b) through the holes into a stainless steel cup (8) at the bottom of the furnace. Optical access to the observation section was facilitated by a quartz window (6). The opposite flange was equipped with an oxygen probe (7) (Australian Oxytrol Systems) with an internal R-type thermocouple to measure the oxygen partial pressure and the temperature close to the alumina tube junction.

The graphite crucible was made of three main parts: a cylindrical hollow shank (3), a crucible hearth (a) and a hollow stopper (d). The shank connected the hearth with a lifting assembly (16) to position the crucible within the vertical alumina tube. The upper end of the graphite crucible was water cooled (17) and had a provision for pressurizing gas inlet and outlet (gas stream G_1). The slag was melted in the hearth section with a capacity of approx. 200 mL (equivalent to approx. 500 g of slag).

At the beginning, the stopper (d) rested on the tapered bottom (c) to prevent molten material (e) to flow through the knife-edged capillary (b). The same capillary was used as in the previous study (1.09 mm inner diameter with a length to diameter ratio of 15 at room temperature). The stopper was connected to a linear precision stepper actuator (18) (Physik Instrumente GmbH, Germany) sitting on top of the furnace. The stopper also housed an alumina sheathed B-type thermocouple (f) to measure the temperature of the melt. The bottom end of the vertical alumina tube was connected to a gas (stream G_4) purged balance chamber (11) via flexible metal bellows (9). A precision balance (Sartorius ED3202S-CW) was used to measure the change in slag weight. On the

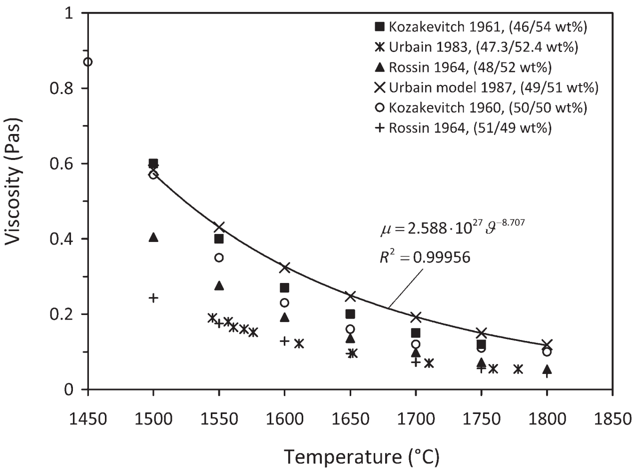

Figure 3. Viscosity of calcia-alumina slag as a function of temperature for compositions close to 50/50 wt %.

Comparison of selected literature data[38,39,43,44] and the values obtained from the Urbain model.[41] A power function which represents the Urbain model values is also given in the figure.

balance stood a graphite stand (10) which held the tapered stainless steel cup (8).

Ultra high-purity argon (BOC Australia) was used as purging and pressurizing gas. Streams G_{2-4} entered the balance chamber and the horizontal tube flanges, and exited at the alumina top flange passing a bubbler (13) for optical verification of overpressure. Stream G_1 pressurized the graphite crucible up to 2 bar using a precision pressure regulator (14) (Norgren, Australia). The pressure differential between the pressurized graphite crucible and the alumina cross tube was measured by a pressure transducer (15) (Sensortechnics, Germany). A pressure relief valve (19), a needle valve (20), and a bubbler (21) completed the assembly.

The slag jets passing through the observable section were filmed with a high-speed camera (4) (Phantom v3.11, Vision Research) with a maximum frame rate of 3250 fps at full resolution (1280 × 800 pixel). The slag at 1600°C was bright enough to record at up to 10,000 fps without any additional lighting. To cover the object distance, a long working distance lens with high magnification was used. IR radiation was blocked with a MidOpt shortpass SP700 hot mirror filter. After recording, the data were transferred from the internal RAM (= 16 GB) within 30 s to the CineMag, a nonvolatile 128 GB storage device. All files were transferred to the hard disc of a computer at the end for further data analysis. The automated image analysis was accomplished with Image-Pro Plus 6.3 (Media Cybernetics).

Pneumatic Vibrator

The external periodic perturbance on the capillary was achieved with a pneumatic turbine vibrator (CVT-P-1 Turbomite by Cleveland Vibrator Co.). A precision pressure regulator ensures a steady rotation speed or vibration frequency, respectively. The mounting position of the vibrator is shown in Figure 2 (item no. 22). It had to be outside the furnace, but as close as possible to the graphite crucible structure to minimize the distance between the source of vibration and the capillary. As both the frequency of vibration and the resulting force exerted by the turbine depend on the structure the vibrator is attached to, a calibration was required to measure the resulting vibration frequency of the graphite capillary. Thereto, the whole setup was assembled and positioned as in the actual experiment, but measurements were performed at ambient temperature as comparable measurements are impossible at high temperatures. A piezoelectric accelerometer was firmly attached to the bottom of the graphite crucible exactly at capillary position (the capillary was removed for this purpose). Then, the parameter frequency, acceleration, and velocity were measured for different air pressures using a VM-6360 vibration meter. The lowest frequency which could be achieved and reliably measured was approx. 120 Hz.

Slag Properties

As in the previous studies, a calcia-alumina slag (49.1/50.9 wt %) was used. The density was estimated from literature values published by Mukai and Ishikawa,[29] and the surface tension σ was taken from own pendant drop measurements. Regarding dynamic viscosity, a look into experimental values available in literature reveals a considerable scatter; see a selection of data in Figure 3 (more data can be found elsewhere[30–37]).

For example, at 1600°C, the deviation can easily exceed 200%. As the fluid dynamic behavior of slag jets is quite sensitive to the dynamic viscosity, it was decided to explore this issue further. For this, the mass flow rate $\dot{M}$ as indicated by the balance was measured for different back pressures or capillary exit velocities, respectively, at 1600 and 1660°C measured by the thermocouple in the slag melt. As the flow is laminar, the mass flow rate can also be calculated with the Hagen–Poiseuille equation with

$$\dot{M} = \frac{\rho \pi R_{\text{cap}}^4}{8 \mu L_{\text{cap}}} \Delta p \qquad (1)$$

In Eq. 1, the capillary radius R_{cap} was set to half of the jet diameter d_{jet} as obtained by image analysis to account for thermal expansion and uncertainty of the capillary diameter during its manufacture. Different models for the viscosity value in Eq. 1 were tested (basically to approximate the assembly to a capillary viscometer), such as the Riboud[40] and the Urbain[41] model, see Kekkonen et al.[42] for an overview. Also, experimental data published by Kozakevitch[43] and Urbain[44] were tested and compared via Eq. 1 with our own experimental data. At the end, the best fit was obtained using the Urbain model. The Urbain model is based on the CaO-Al_2O_3-SiO_2 system and is one of the most widely used models to estimate the dynamic viscosity of slags.[42] Figure 4 shows a comparison between our experimental data for the mass flow rate (symbols) with the mass flow rate predicted by Eq. 1 using the viscosity data from the Urbain model for two temperatures. The main error results from the uncertainty in the determination of the capillary dimensions (inner diameter and length to diameter ratio). The inner diameter was determined by measuring the jet diameter right below the capillary exit. The uncertainty in deciding whether a pixel belongs to the jet or not is 1 pixel. The length to diameter ratio of the capillary is nominally 15, but at high temperature, the correct value is unknown, and the manufacturing process may also yield a slightly different length. Thus, two figures shall illustrate the uncertainty: Figure 4a shows the comparison if the capillary length L_{cap}

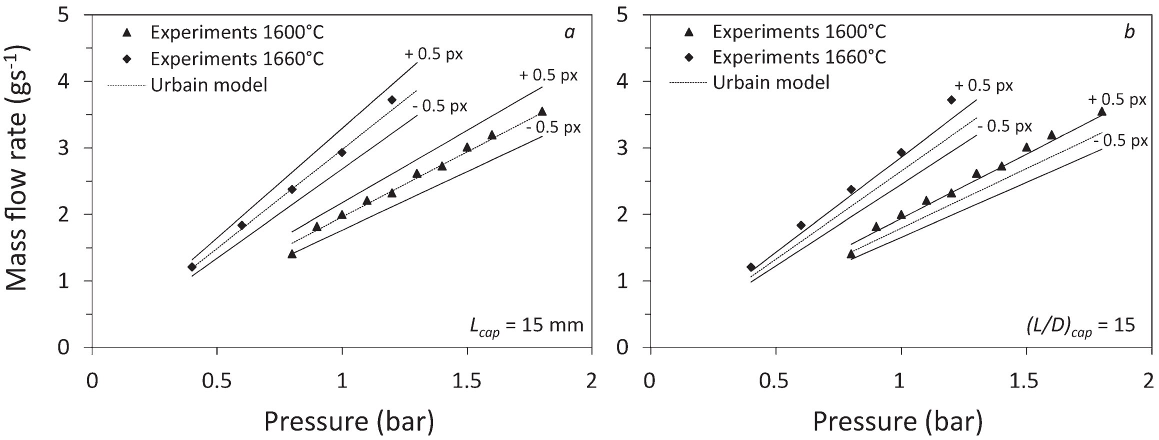

Figure 4. Mass flow rate of calcia/alumina slag as a function of driving pressure difference for different temperatures.

Comparison of experiments (symbols) with Eq. 1 using the viscosity according to the model by Urbain[41] (dashed and continuous lines). The dashed line represents the jet diameter as given in Table 1, the continuous lines represent a jet diameter assuming a ±0.5 pixel error. (a) Length of capillary $L_{\mathrm{cap}} = 15$, (b) $(L/D)_{\mathrm{cap}} = 15$.

is set to 15 mm. The dashed line represents Eq. 1 with the Urbain model values and the diameter as obtained by image analysis. The two continuous lines represent a deviation in the diameter of ±0.5 pixel. The agreement with the Urbain model (dashed line) is very good for both temperatures with a mean deviation below 3%. A pixel of 0.5 produce a 10% deviation from the dashed line. Figure 4b shows the case in which the *L*/*D* ratio of the capillary was kept constant at 15. In this case, the agreement with the dashed line is less satisfactory. However, the experimental values match Eq. 1 within a 0.5 pixel error margin. To conclude, it can be said that the Urbain model represents the experimental data in a satisfactory manner. Hence, the power equation for the Urbain model (see Figure 3) was applied to estimate the viscosity of the slag used in the present study. Table 1 summarizes the physical properties and the jet diameter obtained from image processing at different temperatures.

Overview of Performed Experiments

The furnace was heated to the desired temperature at a heating rate of 5°C min^{-1}. Argon flushed the alumina tubes and the crucible. The graphite stopper closed the capillary. To ensure a uniform temperature, the setup was maintained at experimental temperature for at least 30 min prior to start of experiments. To build up pressure, the crucible gas outlet (20) is closed to a minimum flow rate and the required pressure difference was adjusted. The air pressure for the turbine vibrator was set to the desired value. The stopper was then lifted via the computer controlled linear actuator and the molten slag flowed through the capillary and passed the observation zone. The slag eventually accumulated in the stainless steel cup. The balance recorded the change in mass as a function of time. Pressure difference, oxygen partial pressure, slag bath temperature, and observation zone temperature were also captured by a data logger. Table 2 summarizes the experiments performed in this study. The temperature represents the slag bath temperature. Experiments no. 1–3 were performed at a lower temperature. Those were the first experiments where the functionality of the pneumatic turbine was tested. At that point, a calibration did not yet exist and the frequency was measured with the piezoelectric accelerometer at a flat surface of the lifting assembly. As a reference, no vibration was applied in Experiment 1. In Experiment 2, the turbine speed was zero at the beginning, and then increased manually over a wide range. The frame rate of the camera was lowered to capture a longer sequence to verify that an effect of vibration on the jet could be measured at all. Experiment no. 3 was then performed with a constant frequency. Experiments 4 and 5 were carried out at considerably higher temperature to lower the viscosity and to obtain higher jet speeds. Accordingly, the applied frequency was higher. The calibration was now known. Experiment 4 served as a reference and to calculate the optimum frequency based on the jet velocity. In Experiment 5, the vibration frequency f_{vib} was then adjusted close to the theoretical optimum value, see also next section for more details. As the force and therefore the amplitude increases with rotation speed, frequency and amplitude are not independent for pneumatic turbines. Hence, the frequency was set on the higher side to benefit from the larger amplitude. Besides, the partial oxygen pressure was observed to be rather constant throughout all experiments.

Dispersion Relation

The disturbances always present in an inevitable background noise induce instabilities in a free jet via the capillary. These disturbances may be infinitesimal small and may appear as a complete frequency spectrum.[26] Finally, the jet breaks up close to the frequency which represents the fastest instability growth rate of that noise spectrum. Besides, the amplitude of the disturbance – which is random – also affects the jet instability. As a result, droplet formation from naturally disintegrating jets is unsteady and most likely nonlinear. Our preceding study reports the behavior of naturally

Table 1. Jet Diameter and Physical Properties of Calcia-Alumina Slags at Different Temperatures

ϑ (°C)	ρ (kgm^{-3})	μ (Pas)	σ (mNm^{-1})	d_{jet} (mm)
1570	2753	0.385	589	1.09
1600	2742	0.327	584	1.09
1660	2719	0.237	580	1.12

Table 2. Performed Experiments with External Perturbation (Controlled Breakup)

Experiment no.	ϑ_{slag} (°C)	Δp (bar)	$\dot{M}$ (gs^{-1})	v_{jet} (ms^{-1})	p_{O_2} (10^{-9} atm)	f_{vib} (Hz)	Frame Rate (fps)
1	1570	1.1	1.45	0.57	2.1	0	4000
2	1570	1.1	1.46	0.57	2.6	0…165	1000
3	1570	1.1	1.46	0.57	3.1	140	4000
4	1660	1.2	3.72	1.38	4.2	0	10,000
5	1660	1.2	3.78	1.41	5.1	280	10,000

breaking slag jets and the resulting drop size distributions.[28] One way to increase the uniformity of droplet formation is to impose an artificial disturbance at the capillary at a frequency which corresponds to the maximum growth rate. As the amplitude of natural disturbances is vanishingly small, any deliberately imposed mechanical disturbance is orders of magnitude larger and hence more dominant.[26] To estimate the desired frequency which should theoretically correspond to the fastest growing disturbance, the dependency of the instability growth rate as a function of the wavenumber is required. Thereto, the dispersion relation must be evaluated for the slag system used in the present study. Eggers and Villermaux[12] give an expression for the dispersion relation where higher-order terms were neglected and the Bessel terms expanded. The generalized dispersion relation then reduces to

$$\alpha^2=-\frac{1}{2}\frac{\sigma}{\rho R_{jet}^3}\left[\left(kR_{jet}\right)^2-\left(kR_{jet}\right)^4\right]+(-i\alpha)\frac{3\mu}{\rho R_{jet}^2}\left(kR_{jet}\right)^2 \quad (2)$$

with $i=\sqrt{-1}$, the wavenumber $k=2\pi/\lambda$, and the jet radius at the capillary exit R_{jet}. λ is the wavelength of the instability. In the viscous case, the most amplified wavenumber can be expressed by Eq. 3,[12] in this case with the jet radius R_{jet} as the characteristic length in the Ohnesorge number $Oh=\mu\left(\rho\sigma R_{jet}\right)^{-1/2}$

$$k_{max}R_{jet}=\frac{1}{\sqrt{2+3\sqrt{2}Oh}} \quad (3)$$

Figure 5 shows the dimensionless growth rate $\alpha^*=\alpha\tau$ for slag (according to the physical properties and jet diameter in Table 1 at 1660°C) and water as a function of the dimensionless wavenumber $k^*=kR_{jet}$. τ is the inertial time scale[12]

$$\tau=\sqrt{\frac{\rho R_{jet}^3}{\sigma}} \quad (4)$$

As depicted in Figure 5, the wavenumber which corresponds to the maximum growth rate k^*_{max}, Eq. 3, is 0.57 for slag and 0.7 for water. The corresponding wavelengths are 6.17 and 5.03 mm, respectively. For constant Ohnesorge numbers and jet diameters, the most amplified wavenumber remains the same. The optimum frequency can finally be calculated with $f=v_{jet}\lambda^{-1}$. For example, with $v_{jet}=1.41\ ms^{-1}$ and $\lambda=6.17$ mm, $f=230$ Hz. The frequencies applied in the experiments are given in Table 2.

Results and Discussion

Experiments No. 1–3

Figure 6 shows a sequence of images of a calcia-alumina jet at 1570°C (Experiment 1). The time difference between each image is 5 ms. In this case, no external vibration was applied, hence the jet was in natural breakup mode. Multiple volumes contained in one wavelength of an instability form one droplet. The number of the required instabilities to form one droplet may vary between 1 and 4. The shape is cylindrical for the preponderant part of the jet. Instability waves can be seen close to the jet tip. Yet, from time to time, the jet length changes drastically from around 26 to 10 mm. This happens when an instability wave appears close to the capillary tip. It has more time to grow downstream and may eventually constrict the jet. This causes a large portion of the jet to snap off, see last two images in Figure 6. This snapping creates large main and small satellite droplets. Afterward, the jet recovers, and a new cycle starts. The drop size distribution is relatively wide with a peak at 3 mm. It is also slightly bimodal with a tiny fraction of satellite droplets at around 0.6 mm, created from nonlinear breakup.

Figure 7a shows the jet length of Experiments 1, 2, and 3 as a function of time. As explained above, Experiment 1 represents pure natural breakup. Most of the time, the jet length is close to the value predicted by the following equation[45,46]

$$\frac{L_b}{d_{jet}}=\ln\left(\frac{R_0}{\varepsilon_0}\right)\left[\sqrt{We_{jet}}+3\frac{We_{jet}}{Re_{jet}}\right] \quad (5)$$

with the jet Weber number $We_{jet}=\rho v^2 d_{jet}/\sigma$, the jet Reynolds number $Re_{jet}=\rho v d_{jet}/\mu$, and the term $\ln\left(R_0/\varepsilon_0\right)$ which reflects the ratio of the initial jet radius to the initial disturbance amplitude. Grant and Middleman[45] suggested the correlation $\ln\left(R_0/\varepsilon_0\right)=-2.66\ln\left(Oh\right)+7.68$ to account for the effect of viscosity.

In Figure 7b, the frequency distribution of the jet length shows a nearly Gaussian behavior with the median close to

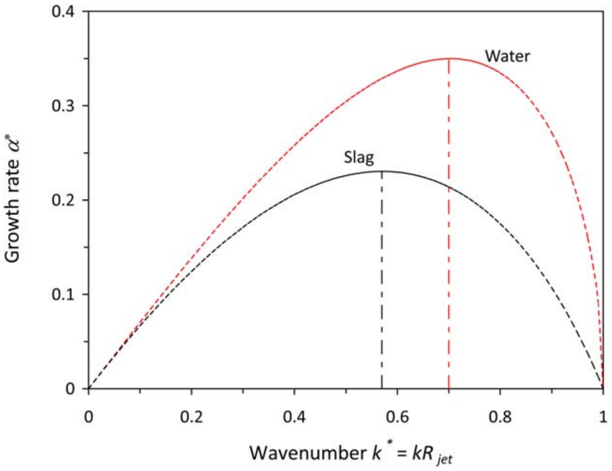

Figure 5. Dispersion relation according to Eq. 2 for water at 20°C and a slag at 1660°C.

Dimensionless growth rate α^* as a function of the wavenumber k^*. The higher viscosity of the slag shifts the most amplified wavenumber to a lower value. [Color figure can be viewed in the online issue, which is available at wileyonlinelibrary.com.]

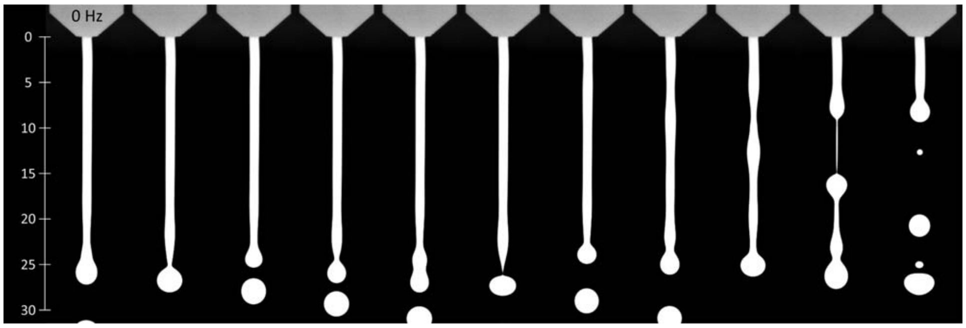

Figure 6. Sequence of a disintegrating calcia-alumina jet at 1570°C in natural breakup mode (Experiment 1).

$Re \approx 5$, $We \approx 1.6$, $Oh \approx 0.4$. The scale at the left-hand side is in mm. Δt between two images: 5 ms.

the value predicted by Eq. 5. The left flank of the distribution is non-Gaussian due to the retracting dynamics. Experiment 2 started identical to Experiment 1 first, but the vibrator frequency was then increased continuously. Accordingly, Figure 7a shows a similar behavior for Experiment 2 in the beginning. The major difference can be observed at around $t=8000\,\mathrm{ms}$. The jet length suddenly decreased to around 15 mm for a period of time significantly longer than that observed in natural breakup mode. The frequency imposed by the vibrator must have reached the resonance frequency of the system. When the vibrator speed was increased further, the frequencies did not match anymore, and soon after, the jet length recovered and reached again the level predicted by Eq. 5. The frequency of Experiment 2 which caused the sudden decrease in jet length was estimated to be around 140 Hz. This frequency was then applied in Experiment 3, and the impact on the jet length is also displayed in Figures 7a, b. The length is decreased to around 17 mm. The behavior is less random and much more regular. The retraction is still visible, but its amplitude is smaller and more due to the fact that the length decreases by a droplet diameter once a droplet detaches. The left flank of the jet length distribution is considerably flatter and thus closer to a normal distribution. It is worthwhile having a more detailed look into Experiment 3, see Figure 8. The regular pattern is obvious. Only a few satellite droplets were observed in total during the whole experiment. Nearly every 50 ms one droplet forms and detaches from the jet. The free end of the jet retracts a bit due to surface tension. But the jet continuously delivers fresh liquid, and the retraction slows down quickly. The jet length recovers to form the next droplet. As shown above, more than just the volume of liquid which is contained in one wavelength flows into the jet tip to form the next droplet. But this time, the number of required wavelength volumes is constant: four. A more detailed look into the jet length vs. time is given in Figure 9a. Note the shape of the curve after one droplet has detached: three steps can be seen in each phase, as exemplarily indicated in one of the patterns by arrows. Each step represents the arrival of one wave instability at the jet tip. The fourth wave delivers the remaining volume required to finally detach the droplet. In the ideal case, it is expected that the volume of fluid present within one wavelength of an instability forms one droplet, or in the nonlinear case a main drop and one or more satellite droplets, depending on the fluid properties and the strength of the disturbance.[10,11]

In Experiment 3, instead, the external vibration imposes a regular "pumping mechanism" in which always the same number of waves is necessary to form and breakup one droplet. Presumably, the imposed vibration frequency matches with the resonance frequency of the system. As indicated by Eggers and Villermaux[12] this may happen if the vibrations produced by the droplet detachment feed back to the container out of which the jet is flowing. The droplet formation frequency is 1/50 ms or 20 Hz, as also revealed by applying a Fast Fourier Transform on the jet length, see Figure 9b. The highest peak is located at 19.7 Hz and represents the droplet formation frequency. This frequency is around three

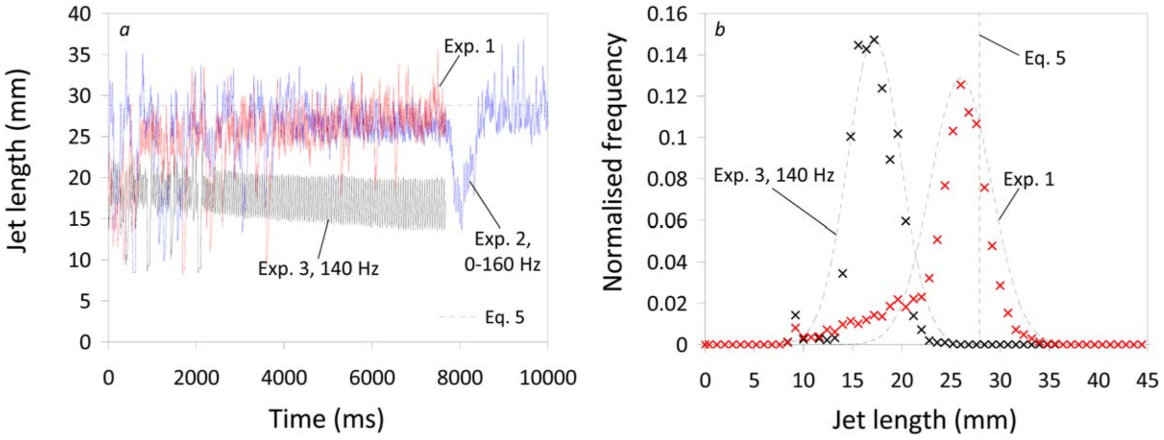

Figure 7. (a) Jet length as a function of time for Experiments 1–3.

(b) Normalized frequency distribution of the jet length for Experiments 1 and 3. In both figures, the dashed line represents the jet length predicted by Eq. 5. [Color figure can be viewed in the online issue, which is available at wileyonlinelibrary.com.]

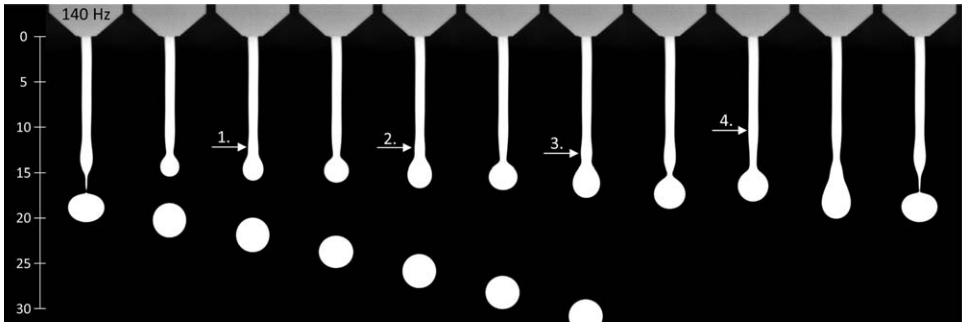

Figure 8. Sequence of a disintegrating calcia-alumina jet at 1570°C excited by an externally imposed vibration frequency of 140 Hz (Experiment 3).

The white arrows indicate the arrival of an instability wave. The fourth wave leads to detachment. The jet length is fairly constant and varies by 1–2 droplet diameters around 17 mm. The size of the detaching droplets is around 3.8 mm. Δ*t* between two images: 5 ms.

times higher than that observed in our previous study for a low speed jet near to the dripping regime in which a similar kind of regularity pattern was observed.[28]

Experiments No. 4 and 5

The jet behavior changes quite substantially if the temperature is increased and the viscosity decreased. Higher velocities and hence higher Reynolds numbers were obtained. The influence of viscosity decreases compared to surface tension, as expressed by a lower Ohnesorge number. In Experiments 4 and 5, the temperature was set to 1660°C. This lead to capillary exit velocities of around 1.4 ms^{-1}, and accordingly $Re \approx 18$. Figure 10 shows a sequence of Experiments 4 (no vibration, Figure 10a) and 5 (with vibration, Figure 10b). When compared to the jets in Figures 6 and 8, it becomes immediately obvious that both jets here (a) are much longer, (b) produce a narrow drop size distribution around a smaller mean size, and (c) show well shaped necks and swells. The latter allows the measurement of the wavelength λ which was found to be around 6 mm. With $k=2\pi\lambda^{-1}$ and $k^*=kR_{\mathrm{jet}}$ with $R_{\mathrm{jet}}=0.56$ mm, the dimensionless wavenumber k^* becomes 0.59. Equation 3 predicted $k^*=0.57$, hence the instabilities in the slag jet in Experiment 5 were growing very close to the predicted maximum growth rate. The jet without vibration in Figure 10a exhibits occasionally nonlinearities in its breakup mode and consequently smaller satellite droplets in the size class 0.7 mm are formed. For the jet exposed to vibration (Figure 10b), no satellites were observed.

The liquid bridge which retracts after droplet detachment may occasionally form a satellite droplet which quickly coalesces with the liquid of the jet tip. The jet length vs. time and the corresponding Fast Fourier Transform are displayed in Figures 11a, b, respectively. The jets in Experiment 4 are in natural breakup mode and show more scatter in the jet length which ranges between 50 and 65 mm. The median value of the corresponding Gaussian distribution (not shown here) is 56 mm. Note that the length is also slightly below the value predicted by Eq. 5, represented by the dashed line in Figure 11a. When vibration is applied, the jet length decreases by 36% to around 36 mm. The jet length is varying in a much narrower bandwidth. The Fast Fourier Transform in Figure 11b shows the frequency spectrum present in the jet length evolution. The first main peak is at a frequency equal to the droplet formation frequency which has increased significantly, compared to the jet of Experiment 3. Instead of 20 droplets/second, this jet creates approx. 250 droplets/second at smaller size, and thus produces a

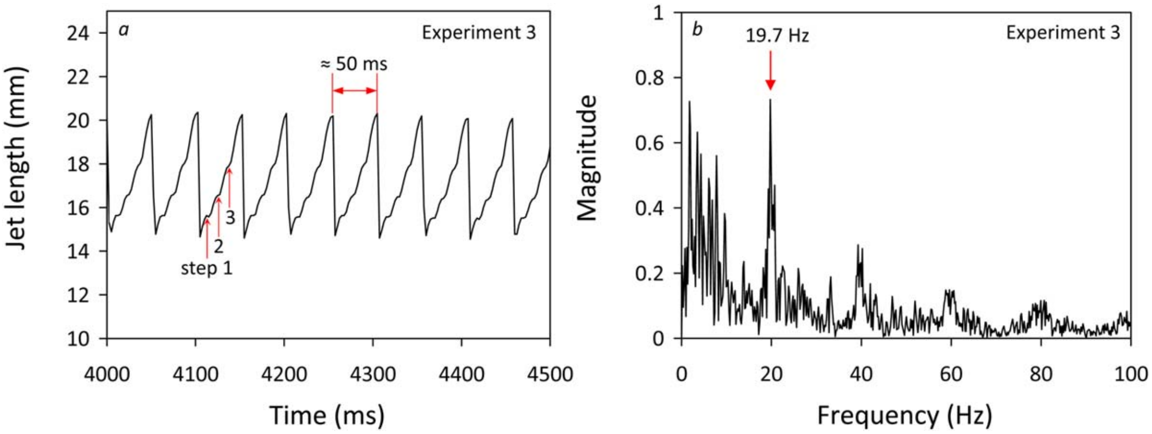

Figure 9. (a) Jet length as a function of time for Experiment 3 (vibration frequency 140 Hz) for a smaller time range. The stepwise pumping mechanism is indicated exemplarily by arrows. (b) Result of a Fast Fourier Transform of the jet length of Experiment 3.

A range of different frequencies can be observed. The most prominent one with the largest amplitude represents the droplet formation frequency of close to 20 Hz. [Color figure can be viewed in the online issue, which is available at wileyonlinelibrary.com.]

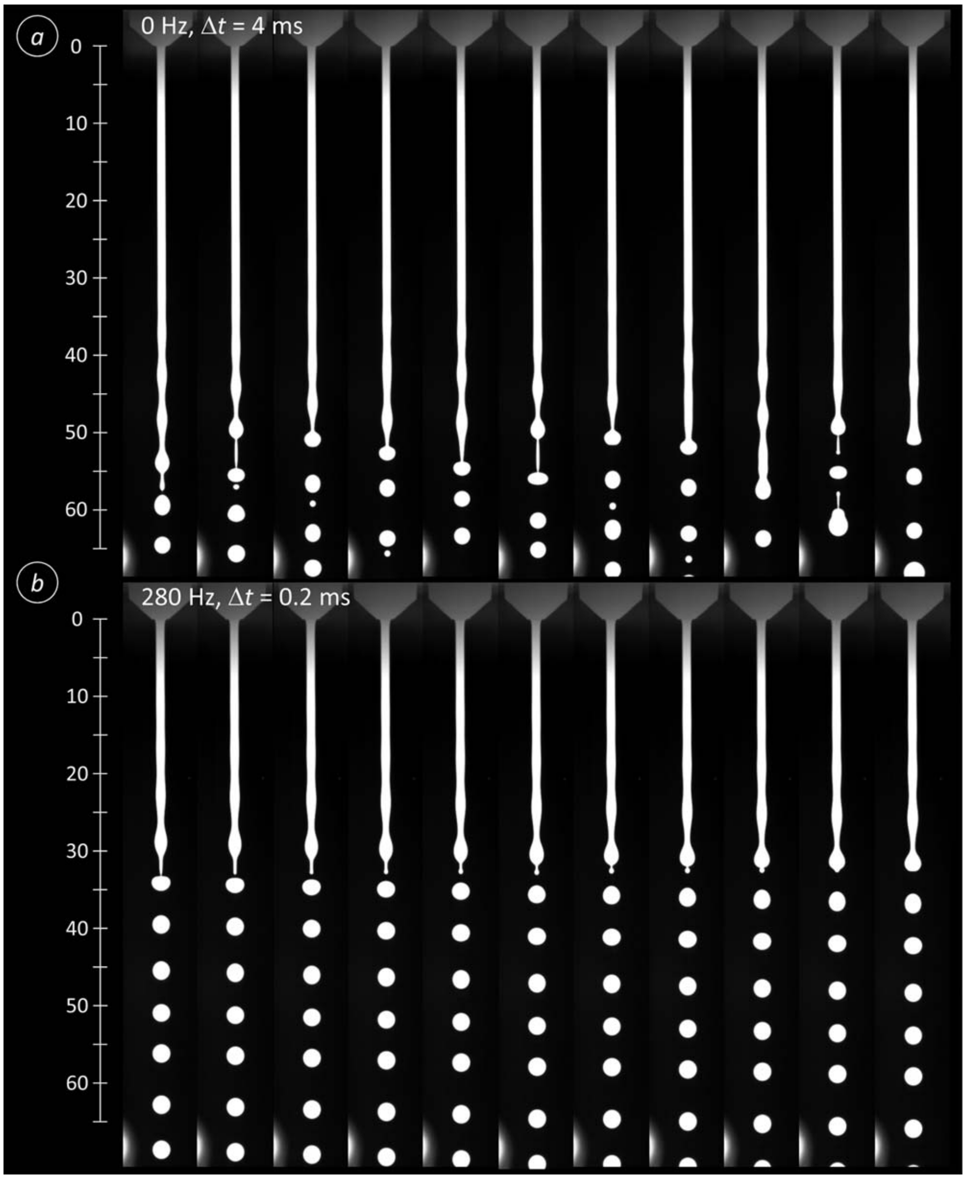

Figure 10. Sequence of disintegrating calcia-alumina jets at 1660°C.

(a) Natural breakup (no external vibration), Experiment 4, $\Delta t = 4$ ms. (b) With external vibration, Experiment 5, 280 Hz, $\Delta t = 0.2$ ms.

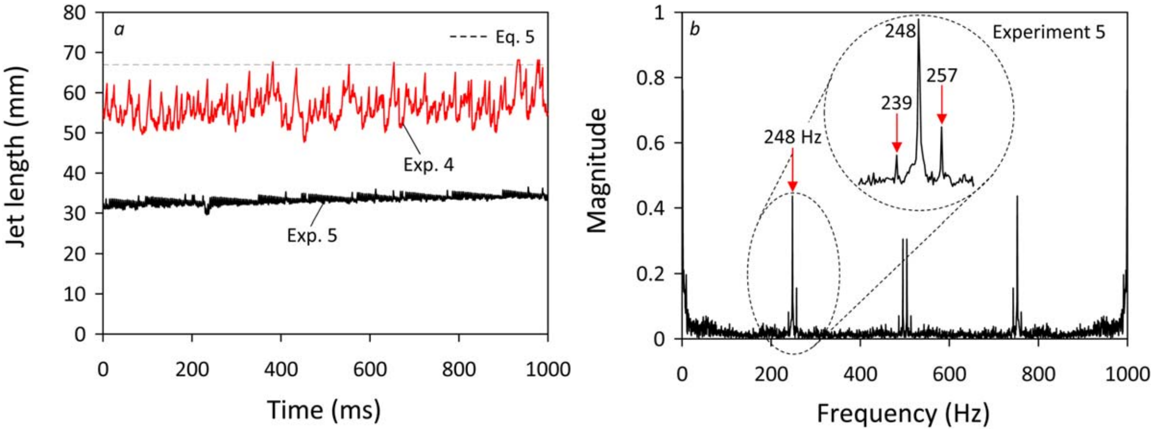

Figure 11. (a) Jet length as a function of time for Experiments 4 (no vibration) and 5 (vibration frequency 280 Hz). Again, the dashed line represents the jet length predicted by Eq. 5. (b) Result of a Fast Fourier Transform of the jet length of Experiment 5.

The first peak with the largest amplitude represents the droplet formation frequency which is 248 Hz in this case. The zoom section shows some minor peaks left and right from the main peak. [Color figure can be viewed in the online issue, which is available at wileyonlinelibrary.com.]

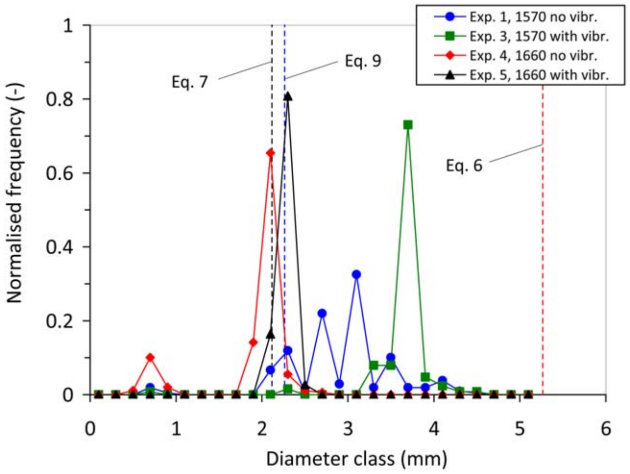

Figure 12. Impact of external vibration on the frequency distribution of droplet sizes for Experiments 1 and 3 (1570°C), and 4 and 5 (1660°C).

Note the suppression of satellite droplets around 0.7 mm for the higher temperature, and the shift toward larger droplet size for the lower temperature case with external vibration. [Color figure can be viewed in the online issue, which is available at wileyonlinelibrary.com.]

larger specific surface area which is beneficial for heat transfer. The main peak has two neighbors which stand out from the background frequencies.

Finally, Figure 12 summarizes the drop size distributions for Experiments 1, 3, 4, and 5. Three vertical dashed lines are also given. The right line represents Tate's law[47] of a single droplet detaching from a capillary assuming balance between gravitation and surface tension

$$d_P = \sqrt[3]{\frac{6\sigma D_{\text{cap}}}{\rho g}} \tag{6}$$

The left line is based on considerations in which one assumes that the volume of one droplet is equal to the volume of the liquid contained in the wavelength of one instability (with the wavelength equal to the distance between two consecutive swells or necks, respectively). The derivation of Eq. 7 can be found in the work by Tyler[10]

$$d_P = 1.89 d_{\text{jet}} \tag{7}$$

Teng et al.[48] argued that the droplet size should depend on the jet and ambient fluid properties. With the definition of the modified Ohnesorge number

$$Oh^* = \frac{3\mu_{\text{jet}} + \mu_{\text{amb}}}{\sqrt{\rho_{\text{jet}} \sigma d_{\text{jet}}}} \tag{8}$$

Equation 9 is obtained which allows estimating the droplet size from low-velocity jets in gases or liquids

$$\frac{d_P}{d_{\text{jet}}} = (1+Oh^*)^{1/6} \left[\frac{3\pi}{\sqrt{2}}\right]^{1/3} \tag{9}$$

Equation 9 reduces to Weber's classical equation for negligible viscosity of the ambient phase, and Oh^* can be replaced by $3Oh$. For the jets used here, $d_P \approx 2.26$ mm which is visualized by the third dashed line in Figure 12. Experiment 1 produced droplet sizes mainly between Eqs. 6 and 7 which reflects the unsteady behavior of this jet. The distribution becomes nearly unimodal and narrow once external excitation comes into play. For the low Reynolds number jet in Experiment 3, the droplet size increases and finds itself in the middle of Eqs. 6 and 7. Experiment 4 is very close to Eq. 7 which underpins the fact that one wavelength forms one droplet. Interestingly, Experiment 5 with external excitation yielded slightly larger droplet sizes than Experiment 4 and is best described by Eq. 9. In addition, this jet suppressed satellite droplet formation which occurred in Experiment 4. Their size is predominantly 0.7 mm which gives a ratio of main droplet to satellite droplet diameter of 3.

Summary and Conclusions

In this study, the effect of external excitation on the breakup of molten slag jets was investigated for different temperatures (1570 – 1660°C) and flow conditions ($Re = 5 - 18$) using a mechanical vibrator. Thereto, the experimental setup from an earlier study[28] was upgraded with a small pneumatic turbine vibrator. The rotation speed and hence the frequency were controlled via a pressure regulator, and a calibration allowed to estimate the required pressure to obtain the desired disturbance frequency at the graphite capillary. The results showed a significant impact of the external vibration on the jet performance. For the lower temperature with lower jet speeds, the jet length decreased significantly. The jet length became more stable and exhibited a regular pattern of droplet detachment, retraction, and recovery. The droplet formation frequency was stable at around 20 Hz. The droplet size increased, and a distinct "pumping mechanism" was established. This may possibly be explained by resonance phenomena as the jets were quite short and the Weber number relatively small which may have allowed the vibrations of jet breakup to feed back to the capillary. Hence, instabilities are not only convected downstream but also upstream. The volume of exactly four wave instabilities was observed to form one droplet. The different stages of "pumping" were identified by image processing. Moreover, the production of satellite droplets was greatly suppressed. However, for a suitable application such as the LDHX, a higher droplet production frequency and a larger specific surface area would be desirable. This was successfully achieved by an increase in temperature (= lower viscosity), an increase in the jet velocity and by applying a frequency close to the theoretical optimum. Again, the jet length decreased considerably, which is crucial for apparatus design. The formation of satellite droplets was hindered. The droplet production frequency increased to approx. 250 Hz, and the droplet size was found to be close to the theoretical value predicted by Tyler's Eq. 7. In contrast to the low speed jet at lower temperature, the faster jet showed ideal behavior: the volume of one instability wave formed one droplet which can be considered as an important step toward the design of a LDHX.

Notation

Latin letters

d_{jet} = jet diameter, m
d_{p} = droplet diameter, m
f = frequency, s^{-1}
g = gravity, m^2s^{-1}
ID = inner diameter, m

k = wavenumber, m^{-1}
k^* = dimensionless wavenumber, $k^*=kR_{jet}$
L = length, m
L_b = jet breakup length, m
$\dot{M}$ = mass flow rate, kg s^{-1}
OD = outer diameter, m
p = pressure, Pa
p_{O_2} = oxygen partial pressure, Pa
Q = volume flow rate, m^3s^{-1}
R_{jet} = jet radius, m
R_0 = initial jet radius, m
t = time, s
UHP = ultra high purity
v = velocity, ms^{-1}
V = volume, m^3

Greek letters

α = growth rate, s^{-1}
α^* = dimensionless growth rate, $\alpha^*=\alpha\tau$
Δp = pressure difference, Pa
ε_0 = initial disturbance, m
ϑ = temperature, °C
λ = wavelength, m
μ = dynamic viscosity, Pas
ν = kinematic viscosity, m^2s^{-1}
ρ = density, kgm^{-3}
σ = surface tension, Nm^{-1}
τ = inertial time scale, $\tau=\sqrt{\rho R_{jet}^3\sigma^{-1}}$

Subscripts

0 = initial, at $t=0$
amb = ambient phase
b = breakup
cap = capillary
g = gas
jet = jet
max = maximum
P = droplet
w = water

Dimensionless numbers

Bo = Bond number, $Bo=\rho R_{jet}^2 g\sigma^{-1}$
Oh = Ohnesorge number, $Oh=\sqrt{We}Re^{-1}=\mu\left(\rho\sigma d_{jet}\right)^{-1/2}$
Oh^* = modified Ohnesorge number, Eq. 8
Re = Reynolds number, $Re=\rho v d_{jet}\mu^{-1}$
We = Weber number, $We=\rho v^2 d_{jet}\sigma^{-1}$

Acknowledgment

The authors thank the Division of Process Science and Engineering of the Commonwealth Scientific and Industrial Research Organisation (CSIRO) for funding through the divisional Capability Development Fund and the postdoctoral research fellowships for M. Wegener and L. Muhmood.

Literature Cited

1. Alam MA, Naser J, Brooks GA. CFD *Simulation of Supersonic Oxygen Jet Behaviour Inside a High Temperature Field*. In: Seventh International Conference on CFD in the Minerals and Process Industries. Melbourne, Australia: CSIRO, 2009.
2. Richardson FD. Drops and bubbles in extractive metallurgy. *Metall Mater Trans B*. 1971;2:2747–2756.
3. Xie D, Jahanshahi S, Norgate T. *Dry Granulation to Provide a Sustainable Option for Slag Treatment*. In: Sustainable Mining Conference. Kalgoorlie, Western Australia, 2010.
4. Wallenberger FT, Weston NE, Motzfeldt K, Swartzfager DG. Inviscid melt spinning of alumina fibers: chemical jet stabilization. *J Am Ceram Soc*. 1992;75:629–636.
5. Bruckner AP. Continuous duty solar coal gasification system using molten slag and direct contact heat exchange. *Sol Energy*. 1985;34:239–247.
6. Goedde EF, Yuen ME. Experiments on liquid jet instability. *J Fluid Mech*. 1970;40:495–511.
7. Amini G, Ihme M, Dolatabadi A. Effect of gravity on capillary instability of liquid jets. *Phys Rev E*. 2013;87:053017.
8. Leroux S, Dumouchel C, Ledoux M. The stability curve of Newtonian liquid jets. *At. Spray*. 1996;6:623–647.
9. Rayleigh L. On the capillary phenomena of jets. *Proc R Soc London*. 1879;29:71–97.
10. Tyler F. Instability of liquid jets. *Philos Mag Ser 7*. 1933;16:504–518.
11. Cheong BS, Howes T. Capillary jet instability under the influence of gravity. *Chem Eng Sci*. 2004;59:2145–2157.
12. Eggers J, Villermaux E. Physics of liquid jets. *Rep Prog Phys*. 2008;71:036601.
13. Wong DCY, Simmons MJH, Decent SP, Parau EI, King AC. Breakup dynamics and drop size distributions created from spiralling liquid jets. *Int J Multiphase Flow*. 2004;30:499–520.
14. Rutland DF, Jameson GJ. Theoretical prediction of the sizes of drops formed in the breakup of capillary jets. *Chem Eng Sci*. 1970;25:1689–1698.
15. Lafrance P. Nonlinear breakup of a laminar liquid jet. *Phys Fluids*. 1975;18:428–432.
16. Pimbley WT, Lee HC. Satellite droplet formation in a liquid jet. *IBM J Res Dev*. 1977;21:21–30.
17. Schneider JM, Hendricks CD. Source of uniform-sized liquid droplets. *Rev Sci Instrum*. 1964;35:1349–1350.
18. Donnelly RJ, Glaberson W. Experiments on the capillary instability of a liquid jet. *Proc R Soc London Ser A*. 1966;290:547–556.
19. Ronay M. Determination of the dynamic surface tension of liquids from the instability of excited capillary jets and from the oscillation frequency of drops issued from such jets. *Proc R Soc London Ser A*. 1978;361:181–206.
20. Orme M, Courter J, Liu Q, Zhu J, Smith R. *Charged Molten Metal Droplet Deposition as a Direct Write Technology*. In: MRS 2000 Spring Meeting, San Francisco, 2000.
21. Liu Q, Orme M. High precision solder droplet printing technology and the state-of-the-art. *J Mater Process Technol*. 2001;115:271–283.
22. Bellizia G, Megaridis CM, McNallan M, Wallace DB. A capillary-jet instability method for measuring dynamic surface tension of liquid metals. *Proc R Soc London Ser A*. 2003;459:2195–2214.
23. Alakoç U, Megaridis CM, McNallan M, Wallace DB. Dynamic surface tension measurements with submillisecond resolution using a capillary-jet instability technique. *J Colloid Interface Sci*. 2004;276:379–391.
24. González H, García FJ. The measurement of growth rates in capillary jets. *J Fluid Mech*. 2009;619:179–212.
25. Rohani M, Jabbari F, Dunn-Rankin D. Breakup control of a liquid jet by disturbance manipulation. *Phys Fluids*. 2010;22:107103.
26. Benda PH. *Experimental Investigation of Droplet Formation with High Temperature Molten Slag*. M.Sc. Thesis, University of Washington, 1983.
27. Wegener M, Muhmood L, Sun S, Deev AV. Novel high-temperature experimental setup to study dynamic surface tension phenomena in oxide melts. *Ind Eng Chem Res*. 2013;52:16444–16456.
28. Wegener M, Muhmood L, Sun S, Deev AV. The formation and breakup of molten oxide jets. *Chem Eng Sci*. 2014;105:143–154.
29. Mukai K, Ishikawa T. Surface tension measurements on liquid slags in CaO-SiO2, CaOAl2O3 and CaO-Al2O3-SiO2 systems by a pendant drop method. *Nippon Kinzoku Gakkaishi*. 1981;45:147–154.
30. Saito T, Kawai Y. On the viscosity of molten slags (I). Viscosity of CaO-SiO2-Al2O3 Slags. *Tetsu to Hagane*. 1952;38:81–86.
31. Evseev PP, Sinyukova LI, Filippov AF. Effect of additions on the melting temperature of slags of the system CaO-Al2O3-MexAy. *Izv Vyssh Uchebn Zaved Chern Met*. 1966;9:74–78.
32. Hofmaier G. Viscosity and structure of liquid silicates. *BHM. Berg- und hüttenmännische Monatsh*. 1968;113:270.
33. Lobzhanidze RB, Filippov AF, Evseev PP. Physico-chemical properties of slags of the system CaF2-MexOy-Cr2O3. *Izv Vyssh Uchebn Zaved Chern Met*. 1970;13:57–60.
34. Povolotskii DY, Mishchenko VY, Vyatkin GP, Puzyrev AV. Physico-chemical properties of melts of the system CaO-Al2O3-CaF2. *Izv Vyssh Uchebn Zaved Chern Met*. 1970;13:8–12.
35. Handfield G, Charette GG. Viscosity and structure of industrial high TiO2 slags. *Can Metall Q*. 1971;10:235–243.
36. Sivkov SL, Suchil'nikov SI, Pavlov VA. Viscosity and electrical conductivity of aluminatitania slags. *Proiz-vo Ferrosplavov*. 1975;4:45–52.

37. Oliveira FA, Miller A, Madías J. Tensión superficial, viscosidad y densidad de algunas escorias CaO-Al2O3. *Rev Metal Madrid*. 1999; 35:91–99.
38. Kozakevitch P. *Viscosity of Lime-Alumina-Silica Melts Between 1600–2100_C, Vol. 7*. In: Proceedings of Metallurgical Society Conference. 1961:97–116.
39. Rossin R, Bersan J, Urbain G. Étude de la viscosité de laitiers liquides appartenent au système ternaire: SiO2-Al2O3-CaO. *Rev Int Hautes Temp*. 1964;1:159–170.
40. Riboud PV, Roux I, Lucas L-D, Gaye H. Improvement of continuous casting powders. *Fachberichte Hüttenpraxis Metallweiterverarbeitung*. 1981;10:859–869.
41. Urbain G. Viscosity estimation of slags. *Steel Res*. 1987;58:111–116.
42. Kekkonen M, Oghbasilasie H, Louhenkilpi S. Viscosity models for molten slag, Vol. 12. Science + Technology. Aalto University, Helsinki, Finland, 2012.
43. Kozakevitch P. Viscosity and structural elements of aluminum silicates. CaO-Al2O3-SiO2 slags between 1600 and 2100°C. *Rev Met*. 1960;57:149–160.
44. Urbain G. Viscosity of silicate melts. *Rev Int Hautes Temp*. 1983;20: 135–139.
45. Grant RP, Middleman S. Newtonian jet stability. *AIChE J*. 1966;12: 669–678.
46. Weber C. Zum Zerfall eines Flüssigkeitsstrahles. *ZAMM J Appl Math Mech*. 1931;11:136–154.
47. Tate T. XXX. On the magnitude of a drop of liquid formed under different circumstances. *Philos Mag*. 1864;27:176–180.
48. Teng H, Kinoshita CM, Masutani SM. Prediction of droplet size from the breakup of cylindrical liquid jets. *Int J Multiphase Flow*. 1995;21:129–136.

Manuscript received Nov. 3, 2013, and revision received Feb. 13, 2014.